MEASUREMENTS OF ATMOSPHERIC WATER VAPOR ABOVE MAUNA KEA USING AN INFRARED RADIOMETER

G.J. Smith[1], **D.A. Naylor**[1], **P.A. Feldman**[2]

[1]Department of Physics, University of Lethbridge,
4401 University Drive, Lethbridge, Alberta, Canada, T1K 3M4
[2]Herzberg Institute of Astrophysics
5071 West Saanich Road, Victoria, British Columbia, V9E 2E7

Abstract

This paper presents the first results from a prototype infrared radiometer which has been developed to measure variations in atmospheric water vapor column abundance from high altitude sites. The performance of the infrared radiometer is compared and contrasted with that of a water vapor monitor operating at radio frequencies. Analysis shows that the infrared radiometer can measure variations at the level of $\sim 1\,\mu$m precipitable water vapor (pwv) in an integration time of 1 s when the total column abundance is ~ 0.5 mm pwv. Since variations in atmospheric water vapor are the dominant source of phase noise in (sub)millimeter astronomical interferometry, an instrument capable of rapid and high sensitivity water vapor measurements has the potential to provide the necessary phase correction information for interferometric arrays.

Keywords: Infrared, Radiometer, Water vapor

1 Introduction

Due to their very large baseline (~ 10 km), high altitude (sub)millimeter astronomical interferometers, such as the Atacama Large Millimeter Array (ALMA) [1], located at an elevation of ~ 5000 m in the Chilean Andes, can, in principle, resolve features on the order of milli-arcseconds when operating at their shortest wavelengths. In practice, the attainable resolution is limited by variations in the line-of-sight water vapor abundance which result in variations in the electromagnetic path length, and hence interferometric phase. One promising approach to the measurement of atmospheric water vapor uses a multi-channel radio frequency (RF) observation of the 183 GHz water vapor emission line [2]. In this technique the telescope antenna simultaneously observes atmospheric water vapor emission along the same line-of-sight as that of the astronomical source. The disadvantages of this method are the risk of RF interference with the sensitive astronomical receivers due to the presence of the 183 GHz local oscillator and the relatively low water vapor signal due to the inherently low radiant emission of the atmosphere in this spectral region and the small spectral bandwidth (1 GHz) of each radiometric channel.

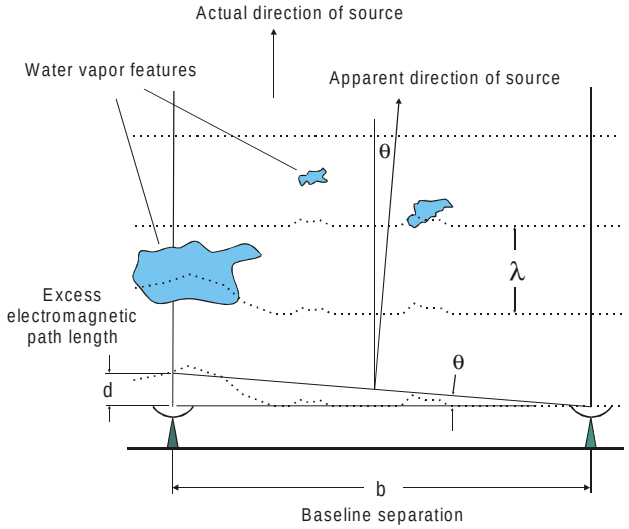

Figure 1: Variation in atmospheric water vapor abundance causes a phase delay of electromagnetic radiation.

In this paper we report the first results from a prototype infrared radiometer [3] which has been developed to measure variations in atmospheric water vapor column abundance from high altitude sites. The infrared radiometer was operated at the James Clerk Maxwell Telescope (JCMT) on Mauna Kea in December of 1999 and its performance is compared and contrasted with that of the JCMT 183 GHz water vapor monitor.

2 Background

The phase delay produced by variations in atmospheric water vapor abundance above a dual element interferometer is shown schematically in Figure 1. The instantaneous apparent angular location of an astronomical source, θ, can be expressed in terms of the baseline of the interferometer, b, and the additional electromagnetic path length, d, or, equivalently, the phase change of the electromagnetic wave, ϕ, by

$$\theta = \frac{d}{b} = \frac{\phi\lambda}{2\pi b}. \tag{1}$$

Carilli and Holdaway [4] have shown that d can be related to the water vapor column abundance, w, expressed as precipitable water vapor (pwv), by

$$d = \frac{1.7\times10^3}{T_{atm}} \times w, \tag{2}$$

where d and w have the same units and T_{atm} is the average atmospheric temperature in K. For $T_{atm} = 260\,K$, the excess path becomes

$$d \simeq 6.5 \times w. \tag{3}$$

This conversion factor has been verified experimentally [5] and is now in widespread use in the radio-astronomical community [6]. Using equation (1), rms variations in column abundance then result in corresponding rms variations in electromagnetic phase given by

$$\langle \phi \rangle = \tfrac{13\pi}{\lambda} \langle w \rangle. \tag{4}$$

The target rms path error for ALMA of $11.5\,\mu$m [7], which corresponds to $\sim 2\,\mu$m pwv, represents a challenging measurement.

3 Motivation for an Infrared Approach

Previous measurements of the atmospheric emission above Mauna Kea, obtained with a Fourier transform spectrometer [8] over the spectral range 455 to 635 cm^{-1}, have demonstrated that over a significant part of this range water vapor is the dominant source of emission. Figure 2 is an excerpt from these data and shows the emission from 455 to 516 cm^{-1} (bottom curves) and computer simulated emission from N_2O, CO_2 and H_2O (upper three curves) modeled for the atmosphere above Mauna Kea. This figure clearly shows that, in this particular region, water vapor is the only source of emission making it one well suited to measurements of atmospheric water vapor.

The advantages of an infrared approach to water vapor measurement are threefold. Firstly, the spectral radiance from atmospheric water vapor is $\sim$three orders of magnitude greater at infrared wavelengths than at radio frequencies and, as shown in Figure 3, for a typical atmospheric temperature of 260 K, is seen to lie near the peak of the Planck function. Furthermore, the spectral bandpass of the infrared radiometer (50 cm^{-1}, 1.5 THz) is seen to be $\sim$three orders of magnitude greater than that of the 183 GHz radiometer. This increased flux can be translated into more sensitive measurements, faster operation, smaller instrument size or some combination thereof. For example, in spite of the much larger surface area of a radio telescope antenna ($\sim$12 m diameter), an infrared radiometer using a primary optic $\sim$10 cm diameter can be shown to receive $\sim$two orders of magnitude more power from atmospheric water vapor emission.

Secondly, at these infrared wavelengths, LN_2-cooled mercury cadmium telluride (MCT) photoconductive detectors can be used. These sensitive, fast and stable devices result in a simple and robust instrument. Thirdly, since an infrared radiometer is an entirely passive device, free of radio frequency interference, it may be placed in close proximity to sensitive astronomical receivers.

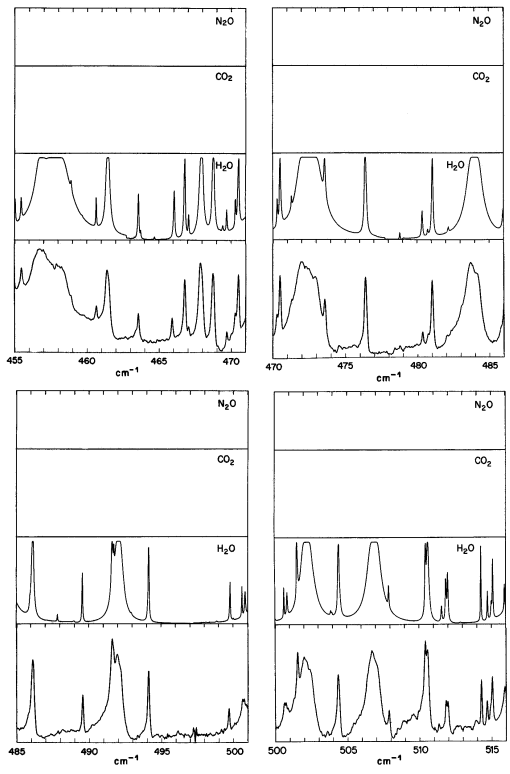

Figure 2: Measured and modelled atmospheric emission spectra in the 20 μm spectral region above Mauna Kea. The lowest trace in each plot is measured emission spectrum. Upper three traces are simulated emission from H_2O, CO_2 and N_2O.

The potential disadvantages of an infrared technique are twofold. The first is that the RF and infrared radiometers sample different atmospheric columns; while the RF beam essentially samples a cylindrical column of atmosphere of area equal to the antenna, the much smaller infrared instrument samples a conical volume determined by its field of view. In an effort to compensate for this difference, the infrared radiometer was designed to sample a patch of sky of diameter equal to that of the radio antenna at a range corresponding to the scale height of water vapor.

The second disadvantage is that emission from ice crystals in cirrus clouds is expected to have a greater impact in the infrared than at radio frequencies. The discussion is complicated by the lack of detailed information on cirrus cloud emission and is a subject of ongoing study. Data presented in this paper show no evidence of the effects of varying emission from cirrus clouds.

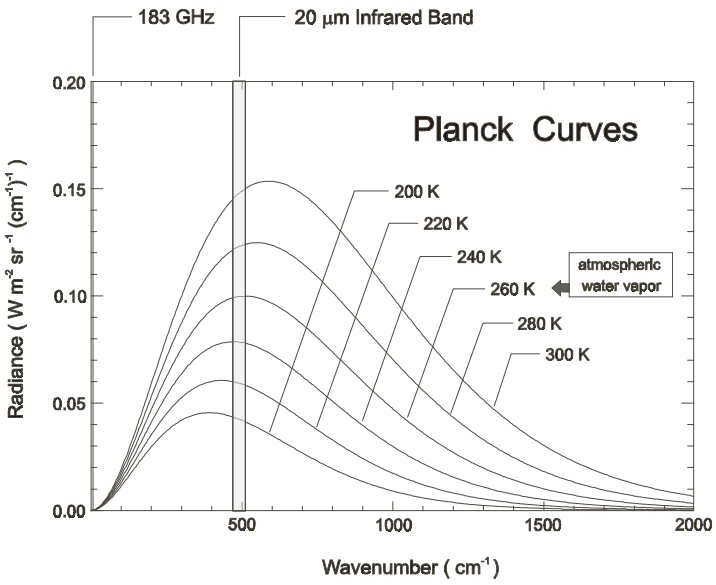

Figure 3: Thermal emission from a blackbody radiator is seen to be three orders of magnitude greater in the infrared than at 183 GHz. For an atmospheric temperature of 260 K, the emission is further seen to lie near the peak of the Planck curve.

4 Instrumentation

While a full description of the infrared radiometer will appear elsewhere [3], the key features of the instrument are presented here. As shown in Figure 4, the radiometer consisted of a LN_2-cooled detector that alternately viewed the atmosphere, and ambient and LN_2 blackbody references by means of a stationary parabolic mirror and a scanning plane mirror. The scanning mirror provided a range of observable zenith angles from 0 to 70.38^o in steps of 0.18^o, corresponding to an airmass range from $1 - 3$. The optical input to the detector was chopped at 200 Hz by a reflective chopper blade so that the detector was alternately presented views of the atmosphere (or the blackbodies) and a reflected view of its own cold environment. The modulated detector signal was amplified by a factor of 2000 and then synchronously detected by means of a lock-in amplifier providing an additional gain of 100. The output from this amplifier was digitized by a 12-bit A/D converter and logged to a data file. A C++ program, running under DOS on a laptop computer, was responsible for instrument control and data acquisition.

The radiometer was operated in two modes, *stare* and *continuous scan*. In the *stare* mode, the scanning mirror was pointed at a fixed zenith angle and data were acquired at a 10 Hz sampling rate. This mode of operation also allowed a direct comparison of the infrared and RF radiometers through a simultaneous

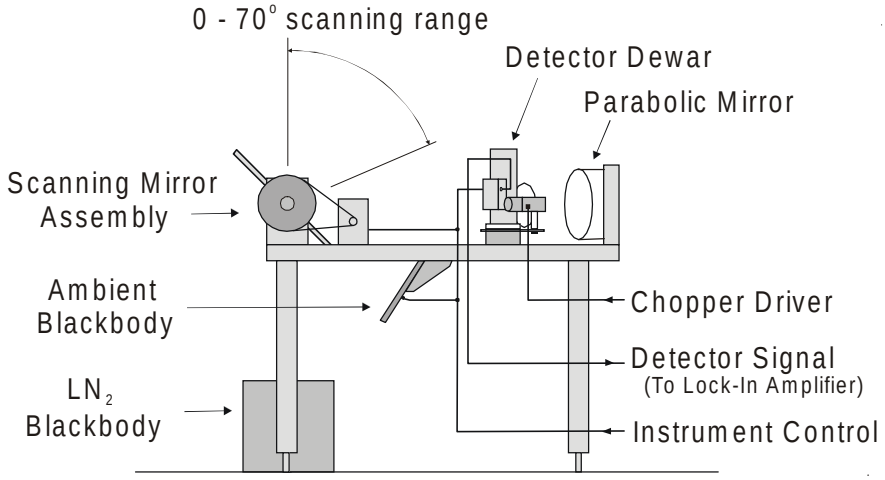

Figure 4: A side view of the infrared radiometer.

observation of atmospheric emission from the same zenith angle. In the *continuous scan* mode, data were acquired over a range of zenith angles from 0 to 70.38^o ($1 - 3$ airmasses), again at a 10 Hz sampling rate. Measurements of the blackbody reference were periodically taken in both modes of operation. A full *continuous scan* cycle consisted of 393 ($70.38^o \div 0.18^o$) measurements from the atmosphere followed by two reference measurements and required ~ 40 s to execute.

Figure 5 shows the infrared radiometer in operation on the apron of the JCMT. Observations were conducted from this location over a five day period from Dec 13 to 17, 1999, typically from 6 p.m. to midnight, local Hawaiian time (LHT).

5 *Stare* Mode Results

5.1 Temporal Variation of Water Vapor

The infrared radiometer was used to obtain high speed observations of the variation of water vapor emission as a function of time along an arbitrary line-of-sight. On Thursday, December 16, between the hours of 12:30 a.m. and 1:10 a.m. LHT, the *stare* mode was used to acquire data from the zenith under the conditions of an apparently clear and cloudless sky for a period of approximately 40 minutes. Figure 6 shows the results of this observation. The complete *stare* observation was composed of three individual *stare* operations, each separated by a period of 10 s and accounts for the two discontinuities in the data seen in

Figure 5: The infrared radiometer, electronics package and laptop control computer on the apron of the JCMT.

the figure at 1150 s and 2300 s.

The data are shown at several magnifications, and at the highest resolution, the individual data points are seen. The instrumental error of ~ 3 mV, determined from a statistical analysis of ~ 200 blackbody measurements, is included in the figure. The signal variation on a time scale of 0.1 s is close to the error limit and may represent real variations in water vapor abundance on these time scales. In any case, significant trends on the order of 1 s are clearly discernible. Of particular interest is the fact that the sky remained clear to the eye during the acquisition of these data.

5.2 Comparison of Infrared and RF Radiometers

On the evening of Friday, December 17, the infrared radiometer was operated simultaneously with the JCMT 183 GHz water vapor monitor. For a period of approximately one hour, the infrared radiometer acquired *stare* mode data from the same direction as the 183 GHz system which utilizes the JCMT antenna itself. The elevation of both instruments corresponded to a zenith angle of 9^o. Since the infrared radiometer was located on the apron of the JCMT, as shown in Figure 5, and the apron rotation is only adjusted periodically to follow the more precise azimuthal antenna rotation, the azimuth coordinates of the two data sets did not correspond exactly.

Upon examination, it was found that there was coherent structure present in the two datasets and that a simple shift in the horizontal axis allowed them to be brought into alignment. Figure 7 shows these results; the lower curve is the

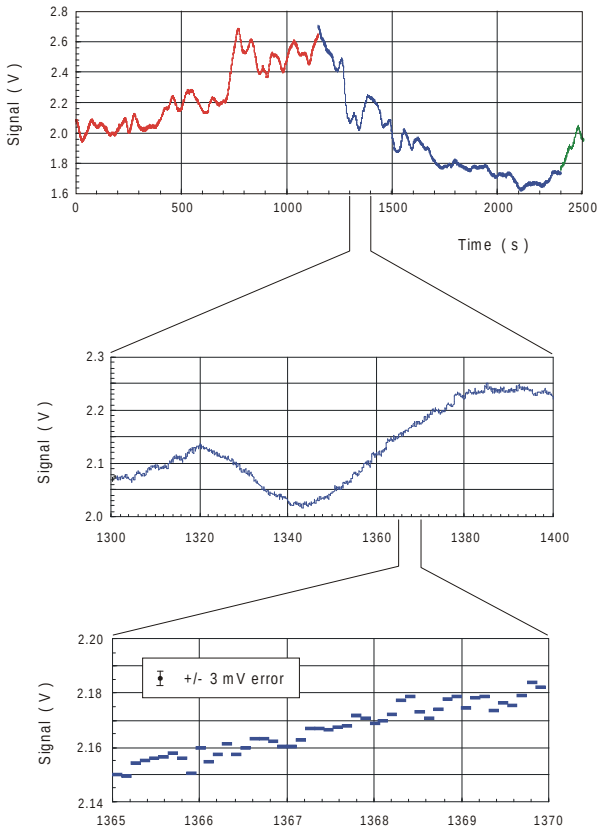

Figure 6: Observation of variations in atmospheric water vapor emission while viewing the zenith in the *stare* mode.

183 GHz data, sampled at a rate of 0.1 Hz. The upper curve is the raw *stare* data from the infrared radiometer, while the middle curve is the same data smoothed by a factor of 10 to an effective resolution of 1 s. The local time shown on the horizontal axis, and the precipitable water vapor scale of the vertical axis, in mm *pwv*, are taken from the 183 GHz data record.

Although not shown in the figure, the vertical axis, labeled in mm *pwv*, has an alternate scale corresponding to the infrared radiometer signal voltage. Given the similarity between these datasets, the 183 GHz data was used to calibrate the infrared radiometer. Each dataset was first smoothed to an effective time resolution of 20 s; the minima and maxima of the two datasets provided two independent calibration points, and are given in Table 1.

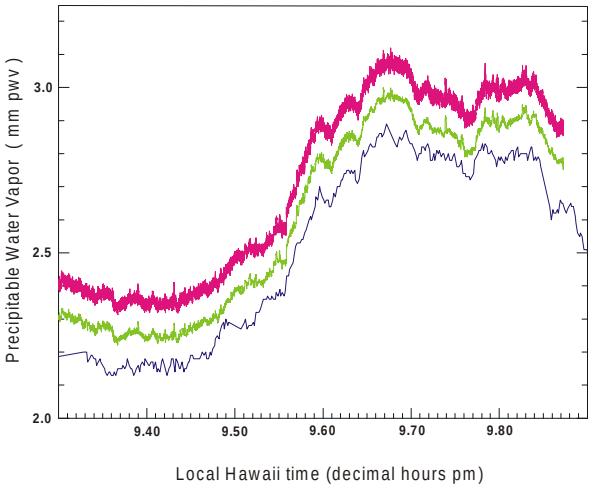

Figure 7: Datasets obtained using the infrared radiometer and JCMT 183 GHz water vapor monitor show good agreement in water vapor abundance as a function of time. The bottom curve is the 183 GHz data. The upper two curves, displaced vertically by 0.1 mm *pwv* for clarity, are data from the infrared radiometer at 0.1 s (top curve) and 1 s (middle curve) resolution. The vertical axis, labeled in *pwv,* refers to the 183 GHz data.

17 December, 1999	Infrared radiometer signal (V_{rms})	183 GHz water vapor monitor column abundance (mm *pwv*)
9.40 p.m. LHT	1.61	2.03
9.67 p.m. LHT	1.94	2.87

Table I

6 *Continuous Scan* Mode Results

6.1 Theory

In order to discuss radiometer performance, it is first necessary to introduce the concept of a *curve-of-growth*. A *curve-of-growth* represents the spectrally integrated emission from an absorbing molecular species as the total amount of that species is varied in a known way. *Continuous scan* datasets obtained by the infrared radiometer were in the form of signal voltage vs. airmass (after conversion of the zenith angles). In order to produce *curves-of-growth* from these datasets, it was necessary to rescale the horizontal (airmass) axes to reflect the column abundance of water vapor in the atmosphere at the time of observation. This was done by establishing a relation between the observed airmass, A, and the absorber amount, u, in units of $\mathrm{kg\,m^{-2}}$. In the case of atmospheric water

vapor, when $A = 1$, the radiometer was viewing the zenith and the absorber amount, u, was simply the vertical water vapor column abundance, w, in units of $\mathrm{kg\,m^{-2}}$, or, equivalently, millimeters of precipitable water vapor, (mm pwv).

At any moment the total absorber amount, u, viewed by a radiometer is

$$u = \int_0^\infty \rho(l)\, dl. \tag{5}$$

If the atmosphere can be considered to be horizontally homogeneous and plane parallel then the instantaneous integrated absorber amount along any line-of-sight is equal to that integrated along the zenith multiplied by the current airmass,

$$u = wA. \tag{6}$$

The signal voltage, V, from a radiometer can be written as

$$V = G(u) = G(wA), \tag{7}$$

where G is, in general, a non-linear function relating the integrated spectral radiance to absorber amount. In the case of a single isolated line, for example, G is the Ladenberg-Reiche function[9]. This equation shows that the radiometer signal is a function of the product of w and A, but is insensitive to how this product is distributed between w and A.

Consider two different atmospheric conditions represented by column abundances w_1 and w_2, where $w_2 > w_1$. *Continuous scan* datasets obtained under these two conditions can be written as

$$V_1 = G(u_1) = G(w_1 A) \tag{8}$$
$$V_2 = G(u_2) = G(w_2 A), \tag{9}$$

where A is the same in both cases since both datasets were necessarily obtained over the same range of zenith angles. If the datasets were each acquired over a short time interval then w_1 and w_2 can be assumed to be constant and equation (9) rewritten as

$$V_2 = G(u_2) = G(w_1 \times \tfrac{w_2}{w_1} \times A) = G(w_1\, A'), \tag{10}$$

where $A' > A$ since $w_2 > w_1$. *Continuous scan* datasets obtained under different column abundance conditions, but over an identical airmass range, can thus be interpreted as having been obtained under the same column abundance conditions but over a larger airmass range. The two datasets lie vertically displaced from one another when plotted on a graph having a common airmass axis from $1-3$ (Figure 8). In light of the above discussion, either one of the two

datasets can then be rescaled horizontally to coincide with the other. This process can be applied to many datasets obtained over a wide range of atmospheric conditions. The vertically displaced curves, plotted on a common graph, could then be interpreted as being different components of a single *curve-of-growth*, obtained by expanding the horizontal scales of subsequently higher curves to produce an overlap with the next lower curve. The horizontal (pwv) range of this composite *curve-of-growth* extends from a minimum equal to the lowest atmospheric column abundance encountered during the observing run (times one) to a maximum equal to the highest atmospheric column abundance encountered times three.

For example, consider two datasets representing atmospheres with column abundances of 1 and 2 mm pwv, respectively, as shown in Figure 8. The *continuous scan* datasets lie vertically displaced from one another when plotted on a graph using airmass on the horizontal scale. When plotted using absorber amount on the horizontal axis, however, the first *continuous scan* dataset would have coordinates from 1 to 3 mm pwv, and the second from 2 to 6 mm pwv. If the upper dataset is rescaled horizontally, it can be made to overlap the first curve over the range of 2 to 3 mm pwv, as shown in Figure 8.

6.2 Constructing the *Curve-of-Growth*

Seven *continuous scan* datasets, representing a range of atmospheric conditions, were chosen to generate a composite *curve-of-growth* as described above. When plotted using the common airmass coordinate, A, each dataset is represented by

$$V_n = G(w_n\, A). \tag{11}$$

The procedure to construct the composite *curve-of-growth* begins by leaving the lowest curve undisturbed; this dataset can be written as

$$V_1 = G(w_1\, A). \tag{12}$$

After the process of rescaling each subsequently higher dataset horizontally to produce an overlap with the previous one, the n^{th} dataset of the composite curve is given by

$$V_n = G(w_1\, \tfrac{w_2}{w_1} \cdots \tfrac{w_n}{w_{n-1}}\, A). \tag{13}$$

An IDL^R routine [10] was developed to determine the scale factors connecting any two datasets. Each *continuous scan* dataset was first re-gridded onto a uniform airmass grid, of spacing $\Delta A = 0.01$, using spline interpolation. The scale factor between any two successive curves, $f = \frac{w_n}{w_{n-1}}$, was found by iteratively adjusting a trial scale factor to minimize the overlap error given by

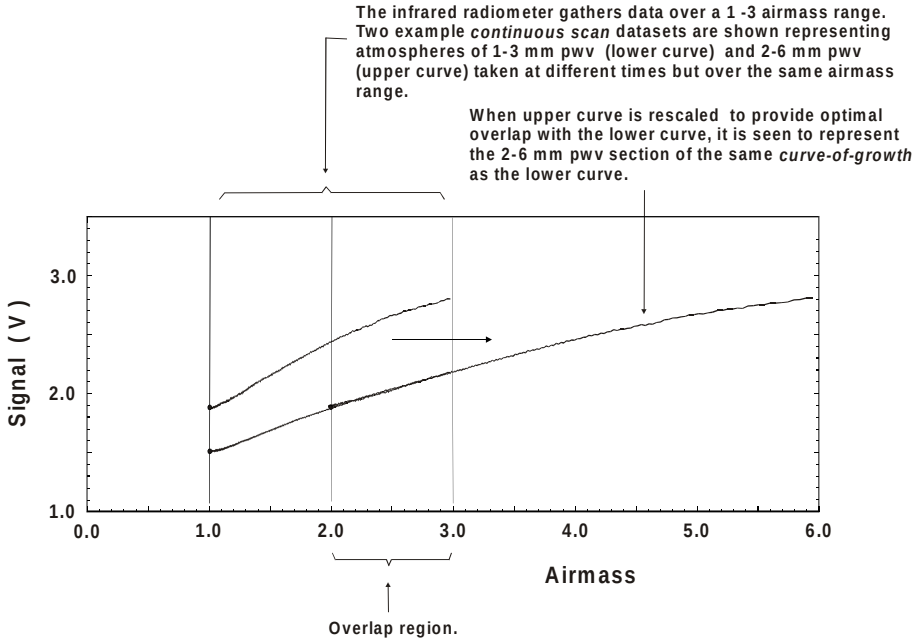

Figure 8: Two *curves-of-growth,* representing different column abundance conditions of the atmosphere but taken over the same airmass range, can be interpreted as components of a single *curve-of-growth* over an extended airmass range. See text for details.

$$\chi^2 = \frac{\sum [a(i) - b(j)]^2}{N}, \tag{14}$$

where a and b refer to the lower and upper datasets being compared. The summation is taken over the overlap region of the two curves. For the case of data taken over an airmass range of $1 - 3$, and a grid spacing of 0.01, equation (14) becomes

$$\chi^2 = \frac{\sum_{100f}^{300} [a(i) - b(fi)]^2}{(3-f)100}. \tag{15}$$

The scaling factor, f, was varied over a range from 1 to 3, in steps of 0.01, and the corresponding χ^2 was evaluated at each step. The optimum scale factor is that which yields the minimum χ^2 value. Figure 9 shows a screen shot of the IDL^R program executing the above procedure for two successive curves. The upper left graph shows two raw datasets plotted over the $1 - 3$ airmass range. In the upper right graph, curve b has been rescaled in the horizontal direction by increasing amounts. The χ^2 of the overlap region is shown in the lower left graph and exhibits a well defined minimum. The lower right graph shows curve b overplotted with curve a using the optimal scaling factor corresponding to the

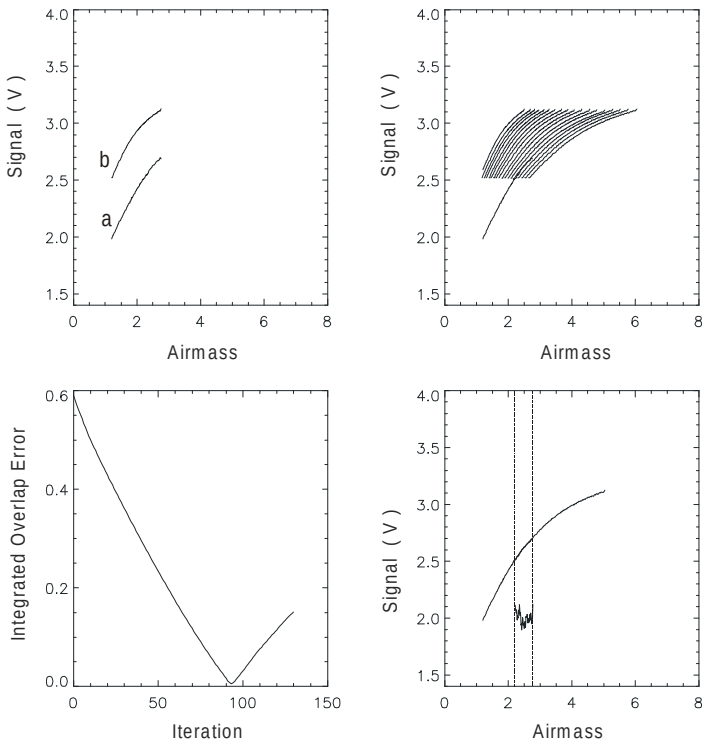

Figure 9: A screen shot of the IDL procedure which iteratively adjusts the horizontal scale factor of the upper *continuous scan* dataset to produce the best overlap with the lower dataset. Upper left graph shows the two raw datasets over the same 1-3 airmass range but representing different water vapor column abundances. Upper right graph shows the iterative horizontal rescaling of curve b. Lower left graph shows the overlap error. Lower right graph shows the fitted curves, the overlap region and the overlap error within this region (multiplied by 10 and displaced vertically by 2 V).

minimum χ^2 value. Also shown in this figure is the difference between the two curves in the overlap region, multiplied by a factor of 10, and offset vertically by 2 V.

Repeating the above process on curve-by-curve basis resulted in the generation of a single, composite *curve-of-growth,* representing the full range of atmospheric conditions encountered during the observing run. Figure 10 shows the final *curve-of-growth* which is composed of seven independent re-scaled *continuous scan* datasets.

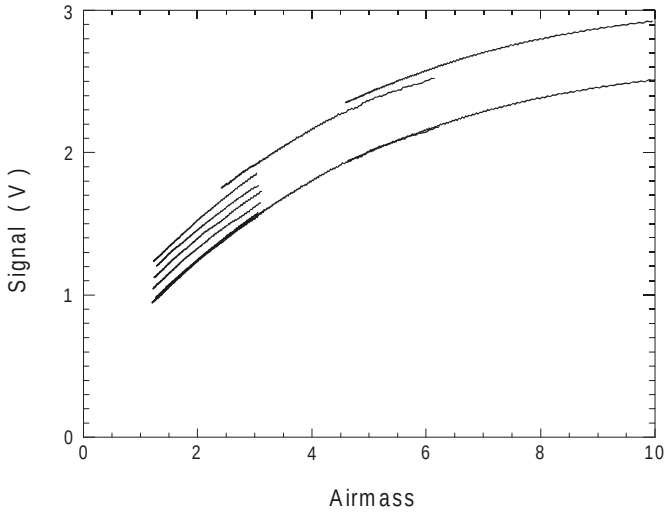

Figure 10: The composite *curve-of-growth (*lower trace*)* is constructed from seven individual curves which are shown successively offset by $\sim$ 0.05 V for clarity.

6.3 Calibration of the Composite Curve

In order to calibrate the infrared radiometer signal, in terms of water vapor column abundance, it is necessary to obtain a simultaneous and independent measurement of atmospheric water vapor. Three independent methods of determining the water vapor column abundance were available. The first method was to use the simultaneous observation of water vapor emission with the 183 GHz JCMT water vapor monitor shown in Table 1. The advantage of this method was that the data represented observations from essentially the same atmosphere at the same time. The disadvantage was that the calibration of the 183 GHz water vapor monitor, in terms of pwv, relies on atmospheric modelling.

The second method was to use measurements of atmospheric opacity provided by the nearby California Submillimeter Observatory (CSO). The CSO has two monitors of atmospheric opacity, one operating at 225 GHz and another at a wavelength of 350 μm. Previous work [11] has shown that the atmospheric opacity at 225 GHz, τ_{225GHz}, is related to the column abundance of water vapor, w, in mm pwv, by

$$w = 20(\tau_{225GHz} - 0.016). \tag{16}$$

Unfortunately, only the 350 μm opacity monitor was operating during this period. However, since the two opacities are related through [12]

$$\tau_{350\mu m} = 23 \times \tau_{225GHz}, \tag{17}$$

equation (16) becomes

$$w(\mathrm{mm}\,pwv) = 20\,(\tfrac{\tau_{350_{\mu m}}}{23} - 0.016). \tag{18}$$

The two principal disadvantages of using the CSO opacity measurements to calibrate the infrared radiometer are that they are obtained from a different azimuthal angle at infrequent time intervals (every 20 minutes).

The third method was to use data provided by radiosondes launched twice daily from Hilo airport at 2:00 a.m. and 2:00 p.m. LHT. There are three principal disadvantages of radiosonde measurements: they occur only once a night, the launch site is $\sim$ 50 km to the southeast of the summit of Mauna Kea and, most importantly, they tend to carry moisture aloft from the tropical launch site which tends to yield elevated column abundance readings.

In light of the above, it was decided to calibrate the infrared radiometer using the data obtained from the JCMT 183 GHz water vapor monitor. Data from the other two methods are included for comparison. The lower curve in Figure 11 is the uncalibrated composite *curve-of-growth* (i.e. Figure 10) plotted in terms of airmass. This curve was transformed into a calibrated *curve-of-growth* by rescaling its horizontal axis to coincide with lowest of the 183 GHz calibration points given in Table 1 (represented by the lower square) and resulted in the upper curve in Figure 11. The second independent 183 GHz calibration point from Table 1 is seen to fall directly on this calibrated curve. The conversion factor between airmass and water vapor column abundance was

$$w = 0.616\,A. \tag{19}$$

The CSO 350 μm data, corresponding to the times of the two 183 GHz calibration measurements in Table 1, were converted to mm *pwv* using equation 18. The resulting values of 1.73 and 2.50 mm *pwv* correspond to radiometer signal voltages of 1.61 V and 1.94 V, respectively. These two data points are plotted in Figure 11 as circles and show good agreement with the 183 GHz data. In fact, the composite *curve-of-growth* could equally well have been calibrated using these two data points had they been of less questionable quality.

Finally, the radiosonde calibration data are displayed in Figure 11 as triangles. These four data points show a wide scatter and a trend toward larger column abundances than the JCMT and CSO data. Unless radiosondes can be launched from the summit of Mauna Kea, the use of such data for purposes of calibration is questionable.

6.4 Infrared Radiometer Performance

If the noise voltage of the infrared radiometer is projected onto the column abundance axis of the calibrated *curve-of-growth*, the sensitivity of the radiometer to changes in water vapor column abundance can be determined. Since the

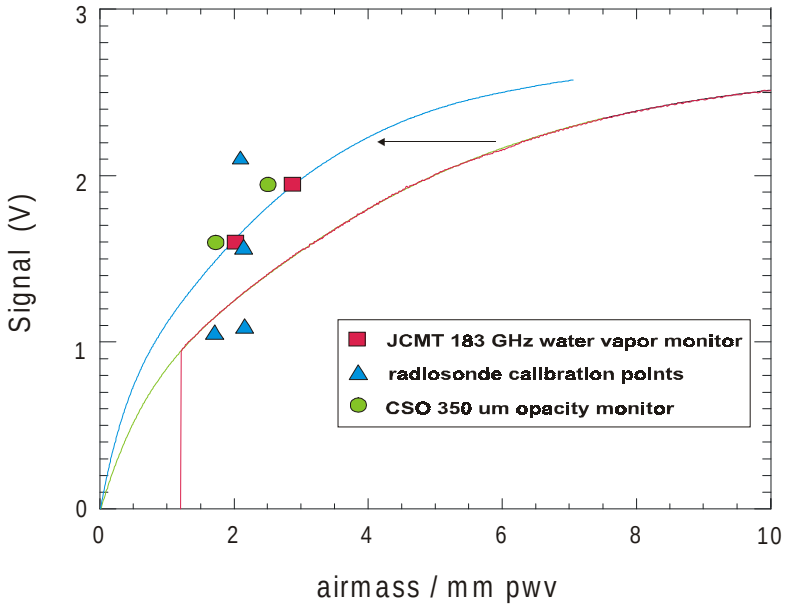

Figure 11: Calibration of the composite curve-of-growth in terms of pwv. The lower curve is the composite curve in Figure 10 referenced to the airmass scale. The upper curve has been calibrated using the lower 183 GHz data point (boxes) and is referenced to the mm pwv scale. The CSO 350 μm calibration points (circles) are seen to suggest a slightly lower column abundances. The radiosonde data (triangles) suggest the opposite.

derivative is itself a function of column abundance, so is the performance of the infrared radiometer; the best performance will be obtained at low column abundance levels where the derivative is larger.

The performance of the infrared radiometer has been evaluated for water vapor column abundances of 0.5 and 1.0 mm pwv, corresponding to very good and average conditions above high altitude observatory sites. The results are summarized in Table 2 in which the resolution values represent a $1\,\sigma$ error in a 1 s integration.

Water vapor column abundance	Curve-of-growth derivative	Radiometer resolution	Electromagnetic path length resolution
(mm pwv)	(V (mm pwv)$^{-1}$)	(μm pwv)	(μm)
0.5	0.99	1.0	6.5
1.0	0.60	1.6	10

Table II

Under conditions of 1 mm pwv, the infrared radiometer has the capability of measuring electromagnetic path length variations of 10 μm. Under conditions of 0.5 mm pwv, this improves to 6.5 μm. This performance satisfies the challenging requirements proposed for ALMA.

7 Conclusions and Future Directions

This paper presents the results from the first field test of an infrared radiometer designed to measure, both rapidly and accurately, the water vapor column abundance above high altitude sites. The results show that the infrared radiometer meets the challenging requirements for phase correction of the new generation of radio interferometers such as ALMA.

Two outstanding issues remain. The first is the effect of the difference between the conical beam of the infrared radiometer and the cylindrical beam of the (sub)millimeter antenna. The second is the impact of cirrus cloud emission on the infrared radiometer measurements. A second generation instrument named *IRMA (*Infrared Radiometer for Millimeter Astronomy), operated remotely over the web from Lethbridge, has been installed at the JCMT. IRMA operates nightly and is currently compiling a database which will allow us to study the infrared emission from the atmosphere above Mauna Kea under a variety of atmospheric conditions and, in particular, the impact of cirrus cloud emission at this wavelength range. Further comparison of IRMA measurements with that from the JCMT 183 GHz water vapor monitor is planned.

8 Acknowledgments

The authors would like to acknowledge the following individuals who have played a significant role in the development of the infrared radiometer project: G.J. Tompkins for electronics support; F. Klassen for machine shop services; I.S. Schofield and Ms. E.A. Pope for software support; Dr. A.A. Schultz for general laboratory support; Drs.L. Avery and J. MacLeod (HIA,NRC) for their interest and continued support for this project; the director and staff of the JCMT for logistical support; Dr. R. Hills (University of Cambridge) for permitting use of the 183 GHz system; and Dr. R. Chamberlin (CSO) for providing the CSO Tau data. DAN acknowledges financial support from NSERC.

References

[1] "The Atacama Large Millimeter Array," http://mma.nrao.edu/ .

[2] M. Wiedner, *Atmospheric Water Vapour and Astronomical Millimeter Interferometry* (PhD Thesis, Cambridge, UK, 1998).

[3] D. A. Naylor and G. J. Smith, "An Infrared Radiometer for the Measurement of Column Abundance and Variability of Atmospheric Water Vapor (in preparation)," Review of Scientific Instruments (2001).

[4] C. L. Carilli and M. A. Holdaway, "Tropospheric Phase Calibration in Millimeter Interferometry," http://www.arXiv:astro-ph/9904248 (1999).

[5] D. C. Hogg, F. O. Guiraud, and M. T. Decker, "Measurement of Excess Radio Transmission Length on Earth-Space Paths," Astron. Astrophys. **95,** 304–307 (1981).

[6] O. P. Lay, "ALMA Memo number 209: 183 GHz Radiometric Phase Correction for the Millimeter Array," http://www.mma.nrao.edu/memos (1998).

[7] R. Hills and J. Richer, "ALMA Memo 303: Water Vapor Radiometers for ALMA," http://www.mma.nrao.edu/memos (2000).

[8] D. A. Naylor, R. T. Boreiko, T. A. Clark, R. J. Emery, B. Fitton, and M. F. Kessler, "Atmospheric Emission in the 20-micron Window from Mauna Kea," pasp **96,** 167–173 (1984).

[9] J. Houghton, *The Physics of Atmospheres, 2nd ed.* (Cambridge University Press, Cambridge, 1986).

[10] "The Interactive Data Language," Research Systems Inc., 4990 Pearl East Circle, Boulder, CO 80301, USA .

[11] G. R. Davis, D. A. Naylor, M. J. Griffin, T. A. Clark, and W. S. Holland, "Broadband Submillimeter Spectroscopy of HCN, NH_3 and PH_3 in the Troposphere of Jupiter," Icarus **130,** 387–403 (1997).

[12] "The CSO Tau monitor webpage," http://puuoo.submm.caltech.edu/ .